Self Consistent Field Theory of isotropic-nematic interfaces and disclinations in a semiflexible molecule nematic

Journal:	*Soft Matter*
Manuscript ID	SM-ART-03-2025-000278.R1
Article Type:	Paper
Date Submitted by the Author:	18-May-2025
Complete List of Authors:	Qing, Longyu; University of Minnesota School of Physics and Astronomy, Viñals, Jorge; University of Minnesota School of Physics and Astronomy

Soft Matter

ARTICLE TYPE

Cite this: DOI: 00.0000/xxxxxxxxxx

Self Consistent Field Theory of isotropic-nematic interfaces and disclinations in a semiflexible molecule nematic

Longyu Qing and Jorge Viñals

Received Date
Accepted Date

DOI: 00.0000/xxxxxxxxxx

A Self Consistent Field Theory description of equilibrium, but non uniform, configurations adopted by semi flexible liquid crystal molecules is presented. Two cases are considered, isotropic-nematic phase boundaries, and topological defects in the nematic phase (disclinations). Nematogens are modeled by worm-like chains, with microscopic interaction potential of the Maier-Saupe(MS) type, with an added isotropic excluded volume contribution. The thermodynamic fields obtained by numerical minimization of the free energy are the molecular density and the nematic tensor order parameter. Interfaces with both homeotropic and planar alignment are studied, as well as biaxiality and anisotropy around $\pm 1/2$ disclinations. The effects induced by fluid compressibility, interaction strength, and elastic anisotropy that follows from chain flexibility on both types of nonuniform configurations are discussed. Defect core sizes decrease as the system becomes less compressible, eventually reaching a constant value in the incompressible limit. The core size is influenced by the nematic interaction strength u_2 and chain persistence length l_p, decreasing as the order increases in the nematic region through manipulation of l_p and u_2. In incompressible limit and for fixed far field nematic order, the core size is seen to be on order of chain contour length for rigid chains, and it decreases as the chains become more flexible.

1 Introduction

Self Consistent Field Theory (SCFT) is a well established technique for the study of the equilibrium properties of polymer and block copolymer melts by computing energy and entropy contributions to the partition function that arise from chain architecture, flexibility, and intermolecular interactions[1,2]. Of particular interest here are studies involving semi flexible chains that assemble into nematic and smectic ordered phases[3–6]. Our analysis is motivated by growing interest in orientationally ordered complex and often active fluids, including bio polymeric systems. While extensive research has been conducted on low molecular weight liquid crystals within both director and tensor order parameter representations, the suitability of phenomenological descriptions such as the Oseen-Frank and Landau-de Gennes (LdG) theories, generally used to describe more complex molecular systems, needs to be established, especially in the presence of topological defects. One possible avenue is the SCFT framework to study not only nematic interactions, but also contributions from chain flexibility, molecular scission and polydispersity, and electrostatic interactions, important features in broad classes of systems of contemporary interest such as lyotropic chromonic liquid crystals, nematic micelles, and bio polymers.

Both Oseen-Frank and LdG models have proven successful in describing small molecule nematics by constructing their free energy as a power series in gradients of the respective order parameters[7]. Expansion parameters are phenomenological, and while well tested for the elasticity of weakly distorted configurations, less is known about the properties near interfaces or topological defects in complex molecular systems. Self Consistent Field Theory offers a potential avenue for the exploration of elasticity and the structure of topological defects in the types of molecular assemblies that are the focus of current active and biological matter research. Existing studies applying SCFT to topological defects have predominantly focused on systems of rod-like molecules under confinement[8,9], while their fine structure and their dependence on chain flexibility remain largely unexplored. Our work presented below is our first step in the direction of modeling defected structures in complex nematic phases, and focuses on the equilibrium configuration of topological defects in a nematic phase comprising semi flexible molecular units.

The free energy of elastic distortion from a uniform nematic phase is given, to lowest order, by three modes of deformation: splay, twist, and bend[7]. The starting point of many theoretical analyses of nematics, however, is the so called one constant approximation according to which splay, twist, and bend elas-

---

School of Physics and Astronomy, University of Minnesota, Minneapolis, MN 55455, USA.

tic constants are assumed to be equal. This renders the nematic elastically isotropic, a reasonably good approximation for small molecule, thermotropic liquid crystals. On the other hand, the response of the so called lyotropic liquid crystals (longer molecule nematogens in solution, where the isotropic to nematic transition is induced by concentration change) is quite different. Broad classes that are being studied at present include lyotropic chromonics[10,11], and nematic micelles[12]. In both cases, the twist elastic constant is as much as one order of magnitude smaller than bend and twist. Such a large contrast gives rise to unexpected phenomenology, including, for example, spontaneous chiral symmetry breaking under confinement[13–17]. Additional research on nematic response in systems with complex molecular units include, for example, actin networks[18], the role of nematic order in cellular mechano adaptation[19], or growth of gliomas in the brain[20]. Theoretical tools are needed to describe potentially defected nematics exhibiting large elastic anisotropy, and with complex molecular architecture and rheology. Given the successes of Self Consistent Field Theory in the polymer field, we begin here by examining the effects of fluid compressibility and molecular flexibility on complex configurations of a nematic phase that involve phase boundaries and topological defects.

In the related case of worm like chains, it is known that both persistence (l_p) and chain contour lengths (L_c) determine the elastic anisotropy of the nematic phase[21]. Polymer field theory work[22] shows that the bend elastic constant (K_3) is larger than the splay constant (K_1) for rigid chains($L_c \ll l_p$), while the splay constants is larger for flexible chains ($L_c \gg l_p$), indicating a crossover between splay and bend contrast as chain flexibility changes. For a wide range of flexibility, the twist elastic constant (K_2) is smaller than both splay and bend[22,23]. In particular, $K_2/K_{1,3}$ becomes negligibly small when $L_c \gg l_p$. Hence, inclusion of nematogen flexibility into the theory naturally leads to elastic anisotropy. In addition to considering chain flexibility, we introduce a molecular interaction potential of the Maier-Saupe (MS) type, supplemented by an isotropic excluded volume term. This allows a simultaneous study of an interaction inducing nematic order, and of fluid compressibility. The MS-type interaction is commonly employed to model orientational ordering in thermotropic liquid crystals, while the Onsager interaction is preferred for lyotropic liquid crystals. In the case of the MS model, the solvent can also be treated implicitly for lyotropic liquid crystals, in which case the excluded volume parameter is interpreted as a renormalized monomer-monomer interaction parameter that accounts for the influence of the solvent molecules[6]. As expected, we find that increasing density favors nematic order. The same effect follows by increasing the persistence length. For the case of an isotropic-nematic interface at coexistence, SCFT correctly predicts biaxiality in the interfacial region when the alignment is planar, and uniaxiality and a wider interface in the case of homeotropic alignment. We also show that the interfacial width increases with persistence length. Disclinations are also correctly reproduced within the theory, including a region of biaxiality near the core, crossing over to a uniaxial core. While the molecular density around the defect core depends strongly on system compressibility and the value of the MS interaction coefficient, the nematic order parameter is largely insensitive to the system compressibility. Finally, the angular dependence of the eigenvalues of the tensor order parameter found around $\pm 1/2$ disclinations is consistent with the elastic anisotropy induced by the semi flexible chains, in agreement with experiments[24], and with calculations based on the singular potential method[25].

2 Self Consistent Field Theory

In this section, and for completeness, we briefly summarize our implementation of the self-consistent field theory (SCFT) for semiflexible molecules with MS interaction. Similar derivations can be found in Ref.[6,26]. The molecules are approximated by worm-like chains characterized by a contour length L_c, and a persistence length l_p. Each chain consists of N_s segments or monomers. For a collection of n worm-like chains confined within volume V at temperature T, the configuration of the i-th chain is described by a space curve $\mathbf{r}_i(s)$, where s $(0 \le s \le 1)$ is a normalized contour variable that denotes the location of a segment along the chain. The unit tangent vector $\mathbf{u}_i(s) = d\mathbf{r}_i/(L_c ds)$ gives the orientation of the segment s. By this definition, the contour length L_c serves as the scale to normalize lengths, making them dimensionless. The microscopic density of segment position and orientation is defined as

$$\hat{\phi}(\mathbf{r},\mathbf{u}) = \frac{V}{n}\sum_{i=1}^{n}\int_0^1 ds\, \delta(\mathbf{r}-\mathbf{r}_i(s))\delta(\mathbf{u}-\mathbf{u}_i(s)) \tag{1}$$

which is dimensionless and satisfies the normalization condition $\int d\mathbf{r}\int d\mathbf{u}\hat{\phi}(\mathbf{r},\mathbf{u}) = V$. For a spatially homogeneous system, the average density $\phi(\mathbf{r},\mathbf{u}) = \langle\hat{\phi}(\mathbf{r},\mathbf{u})\rangle$ is independent of $\mathbf{r}$, where $\langle . \rangle$ denotes a thermal average. Consequently, the normalization condition then implies that the average density, when integrated over all orientations, satisfies $\phi(\mathbf{r}) = \int d\mathbf{u}\phi(\mathbf{r},\mathbf{u}) = 1$. In contrast, for inhomogeneous systems, the local average density at $\mathbf{r}$ may take values that are greater or less than one.

The energy of the system consists of a bending energy of individual nematoges, monomer-monomer interactions and monomer-solvent interactions. The solvent is treated implicitly, and the monomer-monomer interactions are assumed to follow the MS model. The Hamiltonian of the system is given by

$$\begin{aligned}\beta H = &\frac{l_p}{2L_c}\sum_{i=1}^{n}\int_0^1 ds\left|\frac{d\mathbf{u}_i(s)}{ds}\right|^2 + \\ &\frac{1}{2}\frac{n^2}{V^2}\int d\mathbf{r}\int d\mathbf{r}'\int d\mathbf{u}\int d\mathbf{u}'\;\hat{\phi}(\mathbf{r},\mathbf{u})V_I(\mathbf{r},\mathbf{r}';\mathbf{u},\mathbf{u}')\hat{\phi}(\mathbf{r}',\mathbf{u}')\end{aligned} \tag{2}$$

where $\beta = 1/k_BT$, and the kernel function $V_I(\mathbf{r},\mathbf{r}';\mathbf{u},\mathbf{u}') = \delta(\mathbf{r}-\mathbf{r}')\{u_0 - u_2[(\mathbf{u}\cdot\mathbf{u}')^2 - \frac{1}{3}]\}$ in the present study. The excluded volume parameter u_0 quantifies the strength of the isotropic interaction, and u_2 quantifies the strength of the anisotropic MS interaction. The resulting partition function, after a Hubbard-Stratonovich transformation, is

$$Z \propto \int D\phi\int Dw\exp(-\beta F[\phi,w]) \tag{3}$$

with a free energy functional given by,

$$\beta F[\phi,w] = -\frac{n}{V}\int d\mathbf{r}\int d\mathbf{u}\; w(\mathbf{r},\mathbf{u})\phi(\mathbf{r},\mathbf{u}) - n\ln Z_1[w] + n\ln(\frac{n}{V}) + nF_0$$
$$+\frac{1}{2}\frac{n^2}{V^2}\int d\mathbf{r}\int d\mathbf{r}'\int d\mathbf{u}\int d\mathbf{u}'\phi(\mathbf{r},\mathbf{u})V_I(\mathbf{r},\mathbf{r}';\mathbf{u},\mathbf{u}')\phi(\mathbf{r}',\mathbf{u}') \tag{4}$$

where F_0 is a constant that is independent of n and V, and $Z_1[w]$ is the normalized single chain partition function that is a functional of any specified external field $w(\mathbf{r},\mathbf{u})$. Note that this functional, as defined, is non local. Hence the free energy functional of Eq.(4) cannot be written as an integral, over the entire system, of a free energy density. Next, a saddle point approximation assumes that the extremal configurations $[\phi^*, w^*]$ dominate the functional integral defining the partition function, and are defined by,

$$\left.\frac{\delta(\beta F)}{\delta\phi}\right|_{\phi=\phi^*,w=w^*} = 0, \qquad \left.\frac{\delta(\beta F)}{\delta w}\right|_{\phi=\phi^*,w=w^*} = 0. \tag{5}$$

Thus the free energy is approximated by $F[\phi^*, w^*]$. The saddle point approximation yields the relations

$$w(\mathbf{r},\mathbf{u}) = \frac{n}{V}\int d\mathbf{r}'\int d\mathbf{u}' V_I(\mathbf{r},\mathbf{r}';\mathbf{u},\mathbf{u}')\phi(\mathbf{r}',\mathbf{u}')$$
$$= \frac{n}{V}\int d\mathbf{u}'\left[u_0 - u_2[(\mathbf{u}\cdot\mathbf{u}')^2 - \frac{1}{3}]\right]\phi(\mathbf{r}',\mathbf{u}') \tag{6}$$
$$\phi(\mathbf{r},\mathbf{u}) = -V\frac{\delta\ln Z_1[w]}{\delta w}$$

for the two thermodynamically independent fields $w(\mathbf{r},\mathbf{u})$ and $\phi(\mathbf{r},\mathbf{u})$. Notably, the second equation involves solving for a single chain in external field $w(\mathbf{r},\mathbf{u})$

$$\phi(\mathbf{r},\mathbf{u}) = \int_0^1 ds\phi(\mathbf{r},\mathbf{u},s)$$
$$= \frac{1}{4\pi Z_1[w]}\int_0^1 dsq(\mathbf{r},-\mathbf{u},1-s;[w])q(\mathbf{r},\mathbf{u},s;[w]) \tag{7}$$

where the propagator q is a functional of $w(\mathbf{r},\mathbf{u})$, satisfying the modified diffusion equation (MDE)

$$\frac{\partial q(\mathbf{r},\mathbf{u},s;[w])}{\partial s} = \left(\frac{L_c}{2l_p}\nabla^2_{\mathbf{u}} - L_c\mathbf{u}\cdot\nabla_{\mathbf{r}} - w(\mathbf{r},\mathbf{u})\right)q, \tag{8}$$

with initial condition $q(\mathbf{r},\mathbf{u},s=0;[w]) = 1$. The normalized single chain partition function is given by

$$Z_1[w] = \frac{1}{4\pi V}\int d\mathbf{r}\int d\mathbf{u}q(\mathbf{r},\mathbf{u},s=1;[w]) \tag{9}$$

The equilibrium solutions are determined self consistently according to Eqs. 6. It means that the interaction between molecules for a configuration $\phi(\mathbf{r},\mathbf{u})$ creates an effective field $w(\mathbf{r},\mathbf{u})$. This generated field in turn self consistently determines the configuration $\phi(\mathbf{r},\mathbf{u})$. The equilibrium states are obtained when both self consistency conditions are simultaneously satisfied.

The nematic order parameter tensor is obtained from $\phi(\mathbf{r},\mathbf{u})$ through

$$\mathbf{Q}(\mathbf{r}) = \frac{\int d\mathbf{u}\;\phi(\mathbf{r},\mathbf{u})\left(\mathbf{u}\otimes\mathbf{u} - \frac{1}{3}\mathbf{I}\right)}{\int d\mathbf{u}\;\phi(\mathbf{r},\mathbf{u})} \tag{10}$$

where $\mathbf{I}$ is the rank 3 identity tensor. The denominator is needed for normalization in the case of inhomogeneous states where the local density $\phi(\mathbf{r})$ is not uniform.

In order to reduce the computational complexity, we expand all $\mathbf{u}$ dependent quantities in terms of real spherical harmonics[6,27]. The real spherical harmonic expansion of an arbitrary function $f(\mathbf{r},\mathbf{u})$ is written as

$$f(\mathbf{r},\mathbf{u}) = \sum_{l,m} f_l^m(\mathbf{r})\tilde{Y}_l^m(\mathbf{u}) \tag{11}$$

where f can be $q(\mathbf{r},\mathbf{u},s)$, $w(\mathbf{r},\mathbf{u})$ and $\phi(\mathbf{r},\mathbf{u})$. The MDE can then be written in terms of the spherical harmonic expansion as,

$$\frac{\partial q_l^m}{\partial s} = -\frac{L_c}{2l_p}l(l+1)q_l^m - L_c\sqrt{\frac{4\pi}{3}}G_{1ll_2}^{m_\alpha mm_2}\frac{\partial q_{l_2}^{m_2}}{\partial x_\alpha} - G_{ll_1l_2}^{mm_1m_2}w_{l_1}^{m_1}q_{l_2}^{m_2} \tag{12}$$

where the real Gaunt coefficients are defined as $G_{l_1l_2l_3}^{m_1m_2m_3} = \int d\mathbf{u}\tilde{Y}_{l_1}^{m_1}(\mathbf{u})\tilde{Y}_{l_2}^{m_2}(\mathbf{u})\tilde{Y}_{l_3}^{m_3}(\mathbf{u})$[27], the integral of products of three real spherical harmonics over $\mathbf{u}$. The resulting convection diffusion equation for the coefficients is solved with a Lax-Wendroff method[28], with a step size in contour length Δs. The coordinate space is divided into evenly spaced lattice points, (x_i, y_j, z_k). A field $f(\mathbf{r},\mathbf{u})$ is represented by its expansion coefficients defined on lattice points, $f_l^m(x_i,y_j,z_k)$. In the computations below, we restrict the expansion to order $l = 4$. The first equation in the system Eq.(6) leads to linear equations following the expansion[6]

$$w_0^0(\mathbf{r}) = 4\pi u_0\frac{n}{V}\phi_0^0(\mathbf{r}) \qquad w_2^m(\mathbf{r}) = -\frac{4\pi u_2}{5}\frac{n}{V}\phi_2^m(\mathbf{r}) \tag{13}$$

where all other components $l \neq 0,2$ are zero. Therefore, the expansion in real spherical harmonics greatly reduces the number of degrees of freedom of the theory. The expansion also allows us to write the order parameter tensor in terms of the coefficients ϕ_l^m, following the definition in Eq.(10)

$$\mathbf{Q} = \frac{1}{3\sqrt{5}\phi_0^0}\begin{pmatrix} -\phi_2^0+\sqrt{3}\phi_2^2 & \sqrt{3}\phi_2^{-2} & \sqrt{3}\phi_2^1 \\ \sqrt{3}\phi_2^{-2} & -\phi_2^0-\sqrt{3}\phi_2^2 & \sqrt{3}\phi_2^{-1} \\ \sqrt{3}\phi_2^1 & \sqrt{3}\phi_2^{-1} & 2\phi_2^0 \end{pmatrix} \tag{14}$$

where only $l = 0,2$ terms are nonzero due to the definition of $\mathbf{Q}$. The five degrees of freedom for $l = 2$ are sufficient for $\mathbf{Q}$ to describe general biaxial order. As is done often, we parametrize the tensor order parameter as

$$\mathbf{Q} = S(\hat{\mathbf{n}}\otimes\hat{\mathbf{n}} - \frac{1}{3}\mathbf{I}) + P(\hat{\mathbf{m}}\otimes\hat{\mathbf{m}} - \hat{\mathbf{l}}\otimes\hat{\mathbf{l}}) \tag{15}$$

where $\hat{\mathbf{n}}$, $\hat{\mathbf{m}}$ and $\hat{\mathbf{l}}$ are an orthonormal triad of eigenvectors of $\mathbf{Q}$. The director $\hat{\mathbf{n}}$ is the eigenvector with the largest eigenvalue. The constant S is the uniaxial order parameter, and P the biaxial order parameter. Their relationship with the eigenvalues of $\mathbf{Q}$ is, $(\lambda_n, \lambda_m, \lambda_l) = (\frac{2}{3}S, -\frac{1}{3}S + P, -\frac{1}{3}S - P)$.

There are only a limited number of cases in which the propagator q can be obtained analytically, so a numerical solution to the MDE is usually necessary. In this work, in order to find approximate saddle point solutions (Eq.(5)), an iterative method is used with the following steps. Step 1: Define an initial guess for the input fields $w^m_{l(in)}(x_i,y_j,z_k)$. Step 2: Solve the MDE numerically to find the propagator $q^m_l(x_i,y_j,z_k,s;[w^m_l])$, and compute $Z_1[w]$, $\phi^m_l(x_i,y_j,z_k)$, and other thermodynamic quantities accordingly. Step 3: Compute the output fields $w^m_{l(out)}(x_i,y_j,z_k)$ according to the first equation in (Eq.6). Step 4: Define the absolute difference between the input and the output fields to be the error. When the maximum error among all the expansion components and space points is smaller than a given tolerance, i.e., $max(|w^m_{l(out)}(x_i,y_j,z_k)-w^m_{l(in)}(x_i,y_j,z_k)|)<\varepsilon$, the iteration is ended. Otherwise, the input field is updated by using the Picard iteration method[4,5], and going back to step 2. In this work, the contour length L_c is used to nondimensionalize spatial coordinates and system volume, yielding $\tilde{x}=x/L_c$, $\tilde{y}=y/L_c$, $\tilde{z}=z/L_c$ and $\tilde{V}=V/L_c^3$. Accordingly, the dimensionless interaction parameters are given by $\tilde{u_0}=u_0/L_c^3$, $\tilde{u_2}=u_2/L_c^3$. For notational convenience, the tildes are omitted henceforth. The current work obtains numerical solutions using Python, see[29] for further details.

3 Uniform states and isotropic-nematic phase transition

We first briefly review the equilibrium phase behavior provided by the SCFT. We have used $\Delta s=1/100$ in all our calculations. Unless otherwise specified, we set $u_0=10$, $l_p=L_c$, and $n/V=1$ in this section. The normalization condition requires $\phi(\mathbf{r})=1$ and hence $\phi_0^0(\mathbf{r})=1/\sqrt{4\pi}$. Without loss of generality, we consider that the phase transition is from the isotropic phase to a uniaxial nematic phase along the $\hat{\mathbf{z}}$ direction, so that ϕ_2^m is non vanishing only for $m=0$ in the nematic phase. Hence Eq.(14) gives the uniaxial order parameter $S=\sqrt{\frac{4\pi}{5}}\phi_2^0$.

As described in Sec. 2, an iterative method is generally necessary to compute SCFT solutions from an appropriate initial guess. For a uniform configuration, and to the order of approximation in spherical harmonics that we are using, there is a more direct method. There are only two variables that need to be determined, w_2^0 and ϕ_2^0. The dimensionless free energy per chain as a function of w_2^0 and ϕ_2^0 is then given by,

$$\frac{\beta F[\phi_2^0,w_2^0]}{n}=F_0-\ln Z_1[w_2^0]-w_2^0\phi_2^0-\frac{1}{2}\frac{n}{V}\frac{4\pi u_2}{5}(\phi_2^0)^2 \qquad (16)$$

where all constants are absorbed into F_0. The resulting free energy is shown in Fig.1a for $u_2=9.882$, the isotropic-nematic phase transition point. The black solid line illustrates the stationary condition $\frac{\delta(\beta F)}{\delta\phi_2^0}=0$, whereas the dashed line corresponds to $\frac{\delta(\beta F)}{\delta w_2^0}=0$. The saddle points are at the intersections of the solid and dashed lines. The equilibrium free energy per chain along the solid line ($w_2^0=-\frac{4\pi u_2}{5}\frac{n}{V}\phi_2^0$) displays a characteristic double well shape, and it is shown in Fig. 1b for different values of u_2, and as a function of the uniaxial order parameter S. The saddle points corresponds to the minima of this function. The minimum at $S=0$ corresponds to the isotropic phase, and the minimum at $S\neq 0$ corresponds to the nematic phase. The figure illustrates how, as u_2 increases, the global minimum changes from the isotropic phase to the nematic phase, indicating a first order phase transition. The equilibrium uniaxial order parameter S as a function of MS interaction coefficient u_2 can be obtained from the minimum the free energy. The value of u_2 at the phase transition depends on combinations of parameters: Chain number density n/V and ratio L_c/l_p, while it is independent of u_0. Figures 1c, 1d show S as a function of u_2 for different values of n/V and L_c/l_p. As the chain number density increases, the phase transition occurs at a lower value of u_2, while the transition value of the combination u_2n/V remains constant, as indicated by Eq.(6). As the chains become stiffer, the phase transition occurs at a lower value of u_2 (Fig.1d), which is consistent with the result in Ref.[6].

4 Isotropic-Nematic interface

We study next an inhomogeneous configuration with coexisting isotropic and nematic regions, separated by a planar interface. Unlike the case of Sec. 3 in which the density $\phi(\mathbf{r})$ is fixed and uniform in space, the density here is a function of position, and changes across the isotropic-nematic interface. At coexistence, in addition to uniform temperature, the chemical potential $\mu=(\partial F/\partial n)|_V$ and pressure $p=-(\partial F/\partial V)|_n$ need to be the same in both phases. In addition, there is an equilibrium condition associated with free energy minimization with respect to the nematic order parameter. Far from the interface, the nematic phase is assumed uniaxial. Since the order parameter S is unconstrainable, at coexistence one simply has $(\partial F/\partial S)|_{n,V}=0$ in both bulk regions. The equilibrium configuration that contains an interface is obtained as follows: An initial configuration is set up in which $\mathbf{Q}$ and ϕ are fields varying only in the $\hat{\mathbf{x}}$ direction. To model an isotropic-nematic interface, a step function is introduced for S, where $S=0$ on the left side, representing the isotropic phase, and $S\neq 0$ on the right side, representing the nematic phase. The initial value of $\phi_0^0=1/\sqrt{4\pi}$ and $P=0$ are chosen for a uniform density configuration with zero biaxiality. For an arbitrary director direction $\hat{\mathbf{n}}$ in the nematic region, Eqs. (13)(14)(15) are used to compute the initial values of w_l^m. Equations (6) are iterated over a system of length $L_x=10L_c$ with Neumann boundary conditions applied on both ends. In this section we set $u_0=10$, $u_2=9.88$, $l_p=L_c$, and $n/V=1$ unless otherwise specified. The domain $[0,10L_c]$ is uniformly divided into 400 intervals. The iteration process is terminated when the relative maximum errors in w_l^m fall below $\varepsilon=10^{-4}$. The iteration converges slowly if the initial interface is positioned arbitrarily. To accelerate convergence, the interface location is manually adjusted until the error rapidly decreases to 10^{-4}. Although the initial condition assumes a uniform density configuration, a density gap between the isotropic and nematic regions naturally develops during the iteration process for a finite value of u_0. Furthermore, our results reveal the emergence of nonzero biaxiality across the interface under planar alignment, even though the initial condition assumes $P=0$. The nonzero biaxiality is not exclusive to planar alignment but is observed for any alignments where the director is not perpendicular to the interface[4].

First, we study the interface with homeotropic alignment, where the director $\hat{\mathbf{n}}=\hat{\mathbf{x}}$. Density profiles are plotted in Fig.2a for $u_2=9.88$, 10 and 10.2. The local density of the isotropic region

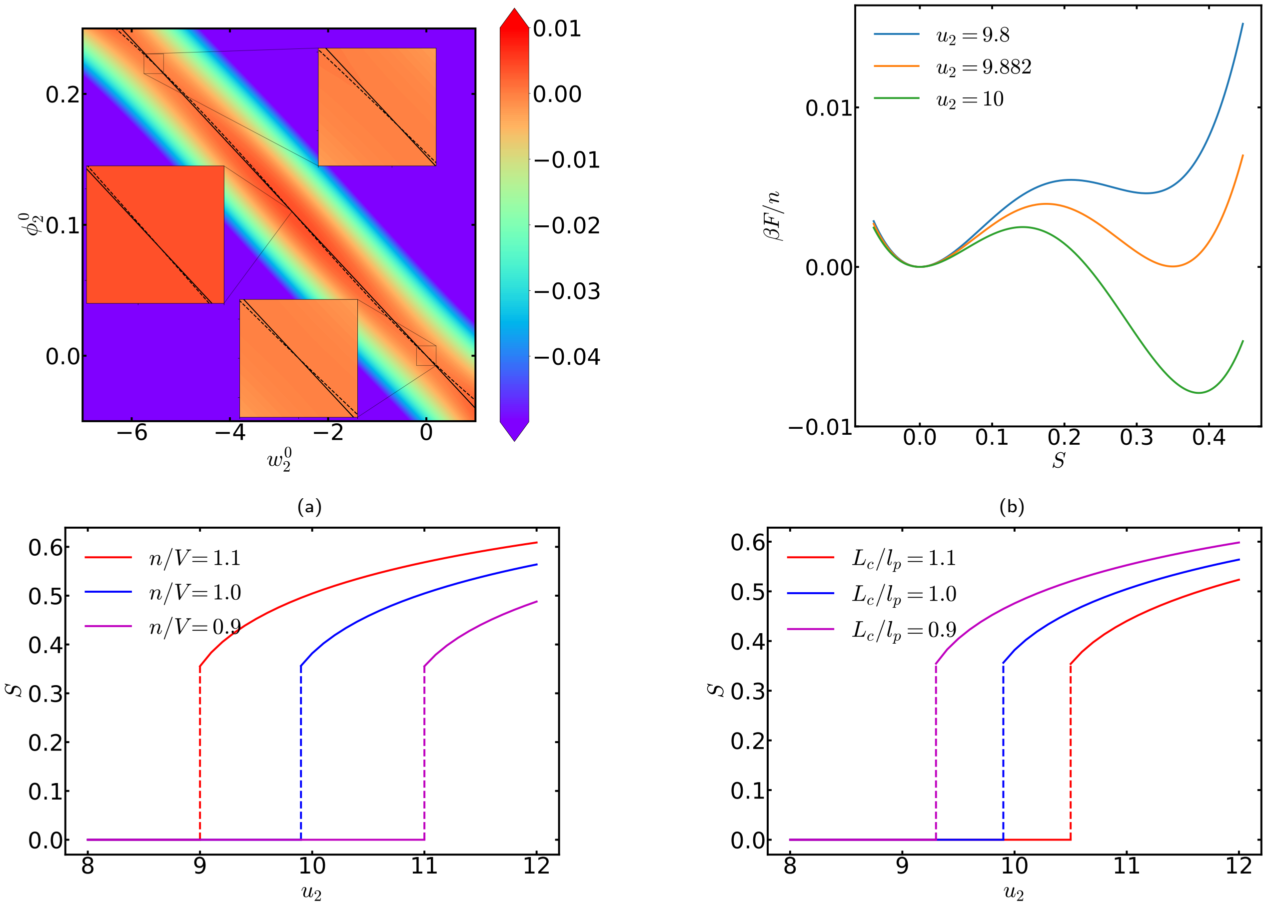

(a) (b)

(c) (d)

Fig. 1 (a), (b)Free energy per chain ($\beta F/n$) of bulk state, where the reference free energy F_0 is chosen to make the free energy of isotropic phase zero. (a) $\beta F/n$ as a function of ϕ_2^0 and w_2^0 at the phase transition (MS interaction strength $u_2 = 9.882$). The black solid and dashed lines correspond to the conditions $\frac{\delta(\beta F)}{\delta \phi_2^0} = 0$ and $\frac{\delta(\beta F)}{\delta w_2^0} = 0$, respectively. The three inset plots provide the enlarged views near the intersections of the solid and dashed lines. (b) $\beta F/n$ along the black solid line in (a) for different values of u_2. (c), (d) Equilibrium uniaxial order S (obtained by minimizing $\beta F/n$ with respect to S) as a function of MS interaction strength u_2 for various chain number densities and flexibilities.

ϕ_I is lower than that of the nematic region, ϕ_N, leading to a density gap between the nematic and isotropic regions. This result is consistent with previous studies[4,30,31]. In the canonical ensemble, with fixed average chain number density n/V, there exists a range of u_2 values for which the isotropic and nematic phases coexist. The relative volume fraction of the nematic and isotropic regions depends on the value of u_2. For higher values of u_2, the nematic region becomes larger but exhibits a lower density. The shift in the interface position is also reflected in the uniaxial order profile, as depicted in Fig. 2b. In order to extract the width (w_i) and location of the interface from our SCFT solutions, we approximate the interfacial uniaxial order profiles by[32]

$$S(x) = \frac{S_N}{2}[\tanh(\frac{x - x_0}{w_i}) + 1] \tag{17}$$

where x_0 denotes the center of the interface, and S_N represents the uniaxial order in the nematic region. The interfacial widths from the density profiles can be extracted in a similar way. Examples of the fits are shown as dashed lines in Fig.2a, 2b and 3a. We find that x_0 from the density profiles is larger than that from the S profiles, indicating that the density jump is displaced towards the nematic side[4]. Additionally, the interfacial width extracted from the density profiles are smaller than that from the S profiles.

We next address how the fluid compressibility, determined by the value of the excluded volume coefficient u_0, affects the interface. By setting $u_2 = 9.88$, the interfaces for different values of u_0 are shown in Fig.2c, 2d. As u_0 increases, the system becomes more incompressible, leading to a reduction in the gaps of both the uniaxial order and the density profiles. The reduction of S_N widens the interface because segregation between nematic and isotropic phases is smaller[33]. In the limit of infinite u_0 (a completely incompressible fluid), the density gaps vanishes, resulting in a uniform density throughout the space, and the interface location is arbitrary.

Interfacial profiles depend on the director angle in the nematic region relative to the interface normal. The results for planar alignment $\hat{\mathbf{n}} = \hat{\mathbf{z}}$ are shown in Fig.3. Unlike the homeotropic alignment case just described, planar alignment is accompanied by nonzero biaxiality near the interface. Near the interface, but on the isotropic side, the component of the tensor order parame-

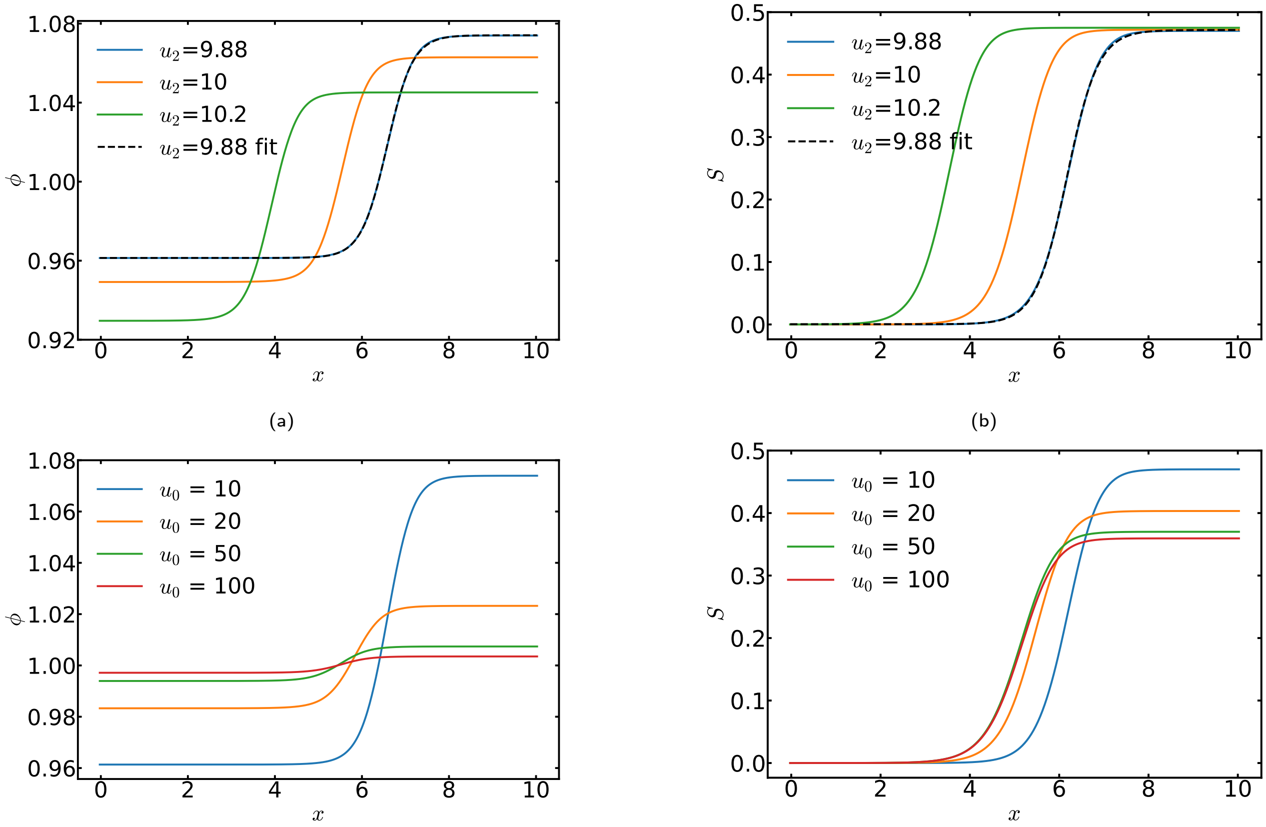

(a) (b) (c) (d)

Fig. 2 Isotropic-Nematic interfaces in (a)(c) density profiles and (b)(d) uniaxial order parameter profiles. (a), (b) Interfacial profiles for various values of MS interaction parameter u_2 (other parameters are set to their default values as described in the Sec.4). The dashed lines represent the fitted profiles obtained using the hyperbolic tangent function (Eq.(17)). (c), (d) Interfaces for various values of excluded volume parameter u_0 (other parameters are set to their default values as described in the Sec.4).

ter Q_{xx} is negative, and $Q_{yy} \approx Q_{zz} > 0$. This is in agreement with predictions from the LdG free energy[32].

Interfacial widths depends on the values of the elastic constants, which, in this model, depends on the flexibility of the chain. To minimize the influence of compressibility on interfacial widths, we consider systems approaching the incompressible limit by imposing $u_0 \gg u_2$. Interfacial widths as a function of chain flexibility L_c/l_p are shown in Fig.4a, where the values of u_2 are chosen to establish a stable interface near the center of the region. Both widths extracted from ϕ and S profiles decrease as the chains become more flexible. In the rigid chain limit ($l_p \gg L_c$), the interface widths are on order of L_c. However, when the chains become flexible, the widths scale with l_p instead. In agreement with existing phenomenology, the interfacial widths in the case of homeotropic alignments are larger than that of planar alignments[4].

In the LdG framework, the elastic free energy density is expressed as a series expansion in gradients of the tensor order parameter

$$f_e = L_1 \partial_k Q_{ij} \partial_k Q_{ij} + L_2 \partial_j Q_{ij} \partial_k Q_{ik} + L_3 Q_{kl} \partial_k Q_{ij} \partial_l Q_{ij} \tag{18}$$

The ratio of interfacial widths for hemeotropic and planar alignments is given by $w_h/w_p = \sqrt{\frac{6+4\kappa}{6+\kappa}}$[32], where $\kappa = L_2/L_1$. Mapping this to the Frank elastic constants for a uniaxial nematic phase with constant scalar order parameter S yields $\kappa = L_2/L_1 = 6(K_1 - K_2)/(3K_2 + K_3 - K_1)$[34]. This relation indicates that the ratio w_h/w_p increases with K_1/K_2. The SCFT solutions show that w_h/w_p increases as the chains become more flexible, as shown in Fig.4b. Consequently, we expect K_1/K_2 to increase with increasing L_c/l_p as well. We verify this hypothesis by estimating the corresponding Frank elastic constants in our model. The dimensionless Frank elastic free energy is[7]

$$\beta F_e = \frac{1}{2}\beta \int d\mathbf{r}\{K_1(\nabla\cdot\mathbf{n})^2 + K_2(\mathbf{n}\cdot\nabla\times\mathbf{n})^2 + K_3[\mathbf{n}\times(\nabla\times\mathbf{n})]^2\} \tag{19}$$

The dimensionless elastic constants are defined as $\tilde{K}_i = \beta K_i L_c$. For convenience, the tildes will be omitted henceforth, as in previous sections. To estimate the elastic constants, we construct configurations with periodic boundary conditions that are predominantly characterized by splay, twist, or bend deformations, respectively. The corresponding elastic free energies are obtained by subtracting the bulk free energy from the free energy of each deformed configuration. We find that all elastic constants decrease as the chains become more flexible, following a trend similar to that of the interfacial widths, as shown in the inset of Fig.4a. Over the tested range of L_c/l_p, the constants K_1 and K_3 are of the same

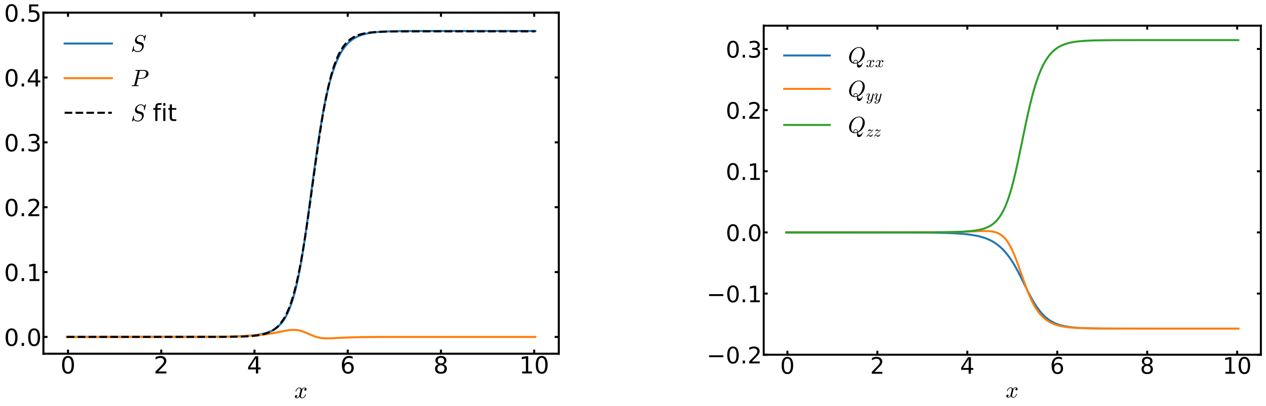

(a) (b)

Fig. 3 Interfacial profiles for planar alignment. (a) Uniaxial order (S) and biaxial order (P) across the interface. The dashed line represent the fitted S profile obtained using the hyperbolic tangent function (Eq.(17)). (b) Three diagonal components of the tensor order parameter as functions of x.

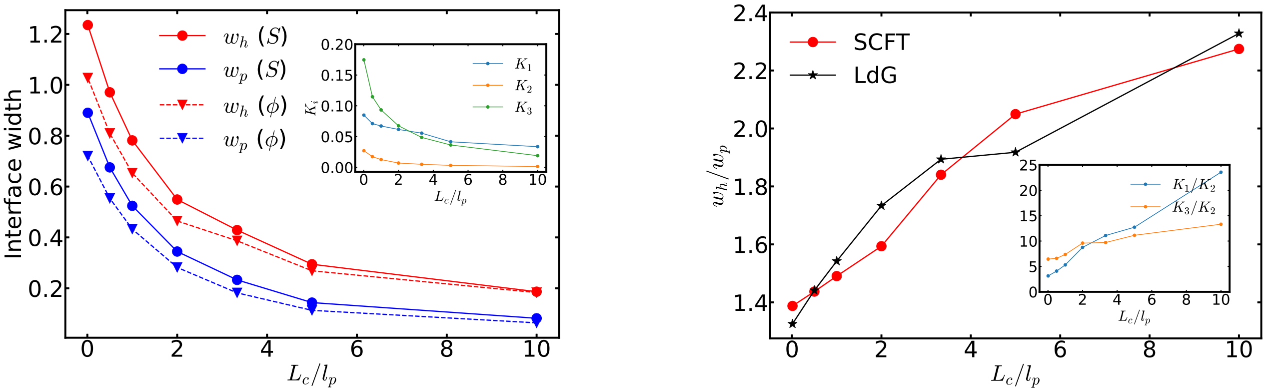

(a) (b)

Fig. 4 Interfacial widths (nondimensionalized by L_c) dependence on flexibility. For different values of ratio L/l_p, the values of MS interaction parameter u_2 are chosen to establish a stable interface near $x = 5$. The values of excluded volume parameter are chosen such that $u_0 \gg u_2$. ($u_2 = 4.58$ for $L_c/l_p = 0.01$; $u_2 = 7.02$ for $L_c/l_p = 0.5$; $u_2 = 9.88$ for $L_c/l_p = 1$; $u_2 = 16.1$ for $L_c/l_p = 2$; $u_2 = 24.7$ for $L_c/l_p = 3.3$; $u_2 = 35.7$ for $L_c/l_p = 5$; $u_2 = 68.4$ for $L_c/l_p = 10$. $u_0 = 100$ for $L_c/l_p = 10$ and $u_0 = 50$ for the rest values of L_c/l_p). Other parameters are set to their default values as described in the Sec.4. (a) Interfacial widths extracted from both the ϕ and S profiles as functions of L_c/l_p for homeotropic and planar alignments. The inset shows the Frank elastic constants as functions of L_c/l_p. (b) Ratio of interfacial widths between homeotropic and planar alignments as a function L_c/l_p. The red line represents the ratio extracted from S profiles, and the black line represents the ratio computed from the elastic constants within the LdG framework. The inset displays the ratios of the elastic constants as functions of L_c/l_p.

order of magnitude, while K_2 is smaller than both and can be one order of magnitude smaller when $L_c/l_p \gtrsim 2$. In the rigid chain limit ($L_c/l_p \to 0$), $K_1 \approx 3K_2$, which agrees with previous studies[22,23]. The ratios among the three elastic constants also vary with chain flexibility. In particular, K_1/K_2 and K_3/K_2 increase with L_c/l_p, as shown in the inset of Fig.4b. Additionally, we computed w_h/w_p from the elastic constants in the LdG framework, as shown in Fig.4b. The results exhibit good agreement with the SCFT solutions, further supporting the consistency between SCFT and the LdG theories. To connect our findings with experimental observations, we further estimate L_c/l_p for lyotropic chromonic liquid crystals based on experimental data[24]. In this system, the interfacial ratio $w_h/w_p \approx 2.1$ was observed, which corresponds to $L_c/l_p \approx 5$ in our calculations. The corresponding elastic constant ratio from the inset of Fig.4b is $K_{1,3}/K_2 \approx 10$, consistent with the experiments that K_1 and K_3 are one order greater than K_2 for lyotropic chromonic liquid crystals[11].

5 Topological defects in two dimensions

We focus here on a different type of non uniform configuration, a topological defect in a two-dimensional square region of lateral dimensions $L_x = L_y = 10L_c$. The region is discretized into 200×200 uniform square domains. Unless stated otherwise, we set $u_0 = 15$, $u_2 = 15$, $l_p = L_c$, and $n/V = 1$ in this section. For the analysis below, we also define polar coordinates (r, φ) relative to the center of the defect. The defect center is defined as the location where $S = P$, and it is determined as part of the free energy minimization. Initially, the disclination center is positioned at the geometric center of the square region. The initial configuration is specified as $S(r) = S_N[1 - \exp(-5r)]$, $P(r) = 0$, and the director angle $\theta = q\varphi$, where $q = \pm 1/2$ is considered in this work. To obtain the SCFT solutions, the iteration process terminates once the

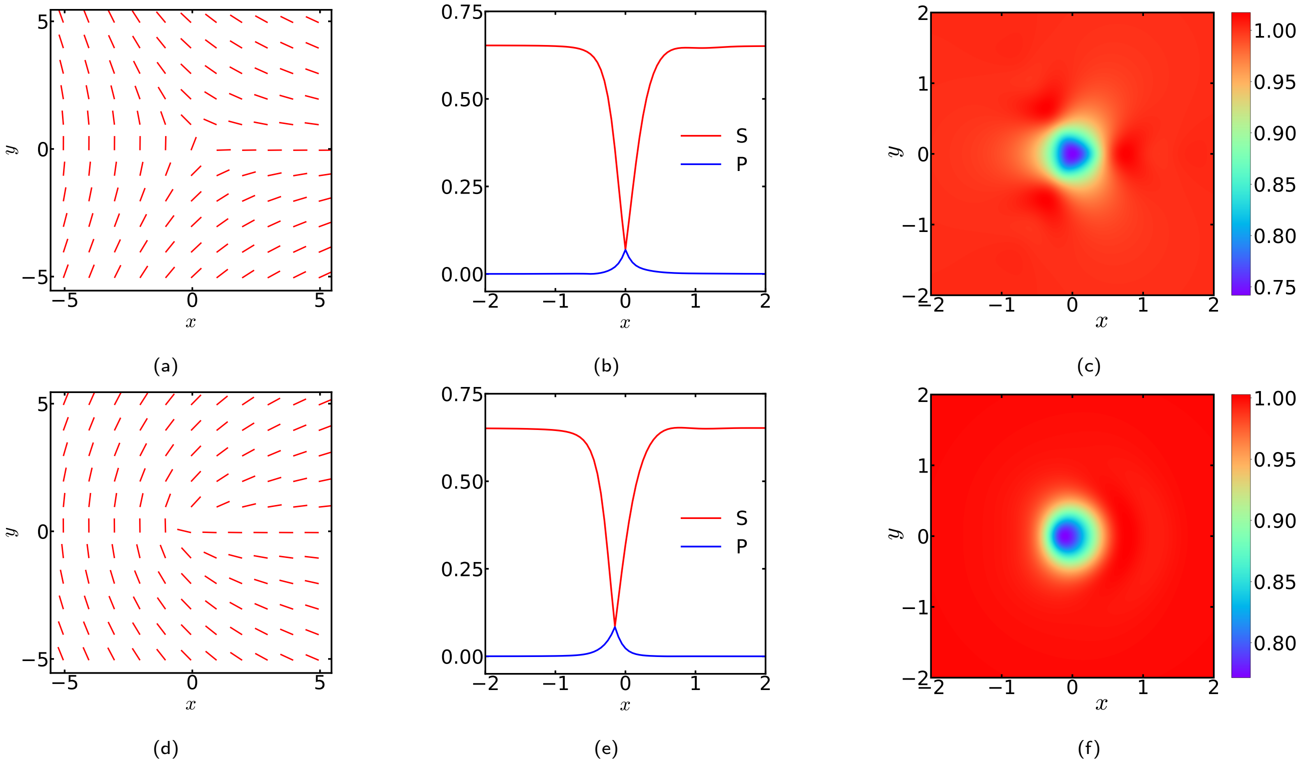

(a) (b) (c)

(d) (e) (f)

Fig. 5 SCFT solutions of ±1/2 defects (x and y are nondimensionalized by L_c). Top: (a), (b), and (c) for -1/2 defect. Bottom: (d), (e), and (f) for 1/2 defect. Left: director fields obtained from the eigenvectors corresponding to the largest eigenvalues of $\mathbf{Q}$. Middle: uniaxial (S) and biaxial (P) order parameters as functions of position x along the line $y = 0$. Right: density (ϕ) fields.

maximum error in the w_l^m field falls below $\varepsilon = 0.01$.

Figure 5 presents the SCFT solutions for $q = \pm 1/2$ defects. The director profiles are shown in Fig.5a and 5d for $q = -1/2$ and $q = 1/2$, respectively. Figures 5b and 5e illustrate the corresponding uniaxial (S) and biaxial (P) order parameters along the line $y = 0$. For $q = -1/2$, the defect core remains at the geometric center. In contrast, for $q = 1/2$, the defect center shifts toward the $-\hat{\mathbf{x}}$ direction as the iterations progress. In both cases, the configurations are uniaxial ($P = 0$) far from the defect core. However, as the defect core is approached, P increases, leading to a locally biaxial configuration. At the exact center of the defect, where $S = P$, the tensor $\mathbf{Q}$ has two degenerate positive eigenvalues, resulting in a uniaxial configuration once again[35,36]. Figures 5c, 5f show the anisotropic density distributions near the defect cores. In both cases, the core regions exhibit lower densities compared to the surrounding nematic regions. Figures 6a, 6d present the distributions of optical retardance, $\Gamma = \gamma(S - P)$ (For simplicity, we set $\gamma = 1$ in the computation), a quantity that can be experimentally measured through polarization microscopy. The Γ distributions reveal cores of smaller extent compared to what would be inferred from the density distributions. Figures 6b and 6e display the density and optical retardance along the line $y = 0$. The density profiles are smooth across the cores, while Γ exhibits singular behavior at the cores. It is noteworthy that, in the case of $q = -1/2$, the location of lowest density coincides with the defect core center. However, for $q = 1/2$, the location of the lowest density does not align with the defect core center. The Γ distributions are further analyzed by their angular Fourier modes $\Gamma(r, \varphi) = \sum \Gamma_n(r)\cos(n\varphi)$, as shown in Fig.6c and 6e. The anisotropic terms, Γ_1 in 1/2 defect and Γ_3 in $-1/2$ defect, reflect the anisotropy in the splay and bend elastic constants. The radial dependence of these terms is consistent with previous experimental and theoretical studies[24,25].

We finally examine the dependence of the core structure on the interaction coefficients u_0 and u_2, as well as on chain flexibility. Figure 7 presents the density profiles (top) and optical retardance (bottom) along $y = 0$ for a $q = -1/2$ defect under varying parameters. For each plot, all parameters are held constant($u_0 = 15$, $u_2 = 15$, $l_p = L_c$, and $n/V = 1$), except for the specific parameter being examined. We observe that the compressibility parameter u_0 does not affect nematic order (S_N) in the nematic region. The core radius decreases as the system become less compressible and reaches a plateau in the incompressible limit. However, S_N shows an increase with u_2 and l_p, as expected from the bulk state study. The density difference between the defect core and the nematic regions decreases as the system becomes less compressible (i.e., with increasing u_0). Increases in u_2 or l_p lead to greater order (S_N) in the nematic region and an increased density difference between the defect core and the nematic regions. However, while an increase in u_2 expands the region of density variation, the size of density variation region remains relatively unchanged when l_p is increased. To quantitatively analyze the size of the core from the Γ configurations, we replotted Fig.7e and 7f in Fig.8a and 8b by normalizing the data using the optical retardance in the nematic region (Γ_N) and a characteristic length ξ, defined such that $\Gamma(x = -\xi, y = 0) = \Gamma_N/2$. It allows ξ to be displayed as a function

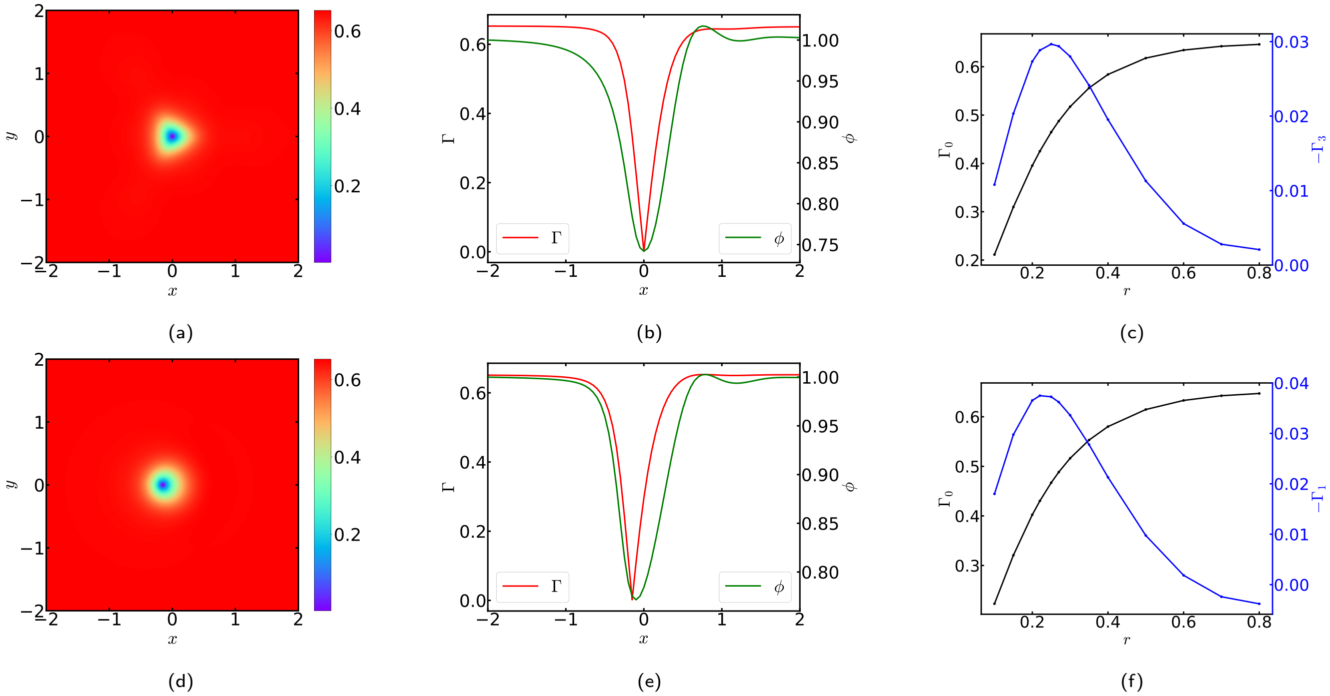

Fig. 6 SCFT solutions for $\pm 1/2$ defects (x, y and r are nondimensionalized by L_c). Top: (a), (b), and (c) correspond to a -1/2 defect. Bottom: (d), (e), and (f) to a 1/2 defect. Left: spatial distributions of optical retardance (Γ). Middle: Γ and the ϕ as functions of position x along the line $y = 0$. Right: Fourier components of Γ as functions of the radial distance from the defect center.

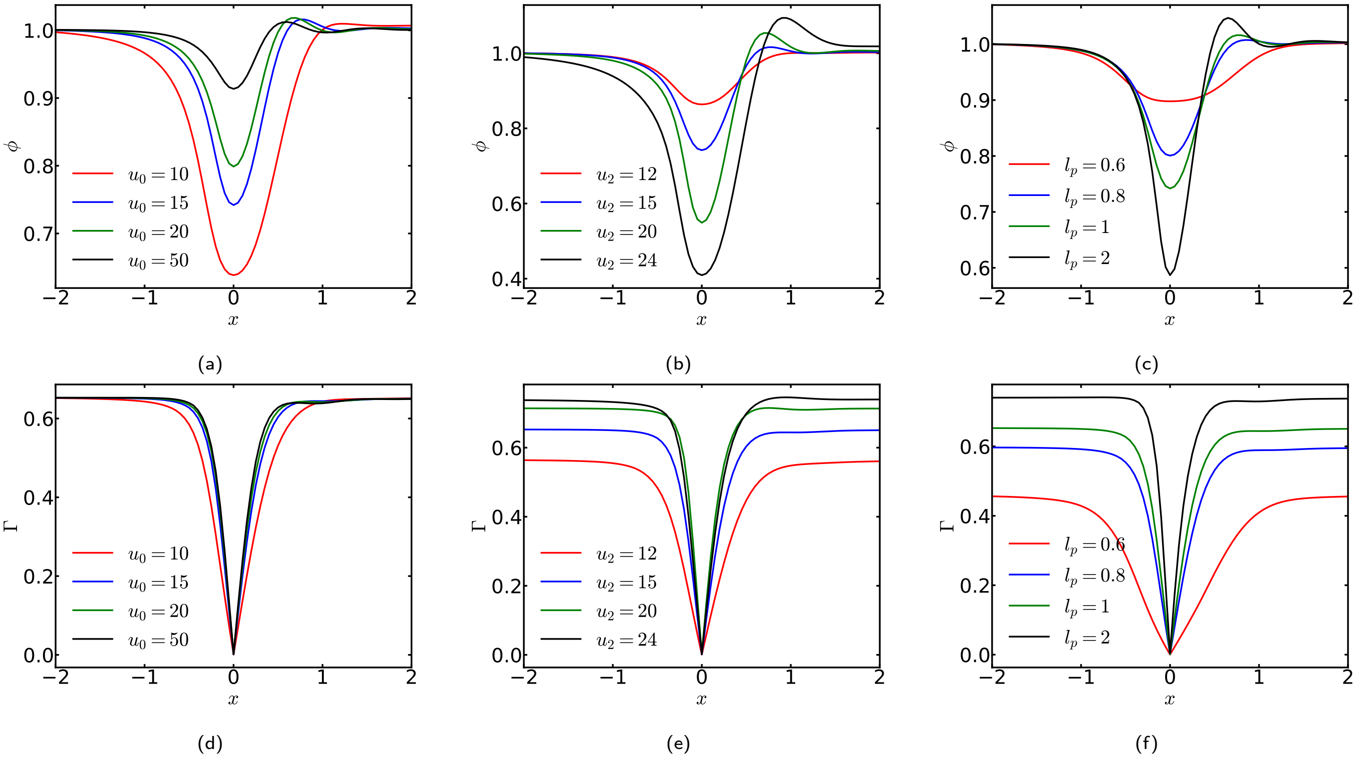

Fig. 7 Density (ϕ) and optical retardance (Γ) along the line $y = 0$ for $-1/2$ defect at varying values of (a)(d) excluded volume parameter (u_0), (b)(e) MS interation parameter (u_2) and (c)(f) persistence length (l_p). For each plot, all parameters except the one being varied are set to their default values as described in the main text. Coordinate x is nondimensionalized by L_c.

of u_2 and l_p, as shown in Fig.8d and 8e. The characteristic length ξ decreases with increasing u_2 or l_p, accompanied by an increase in Γ_N. The point for $u_2 = 24, u_0 = 15$ appears anomalous due to its coupling to a wide density variation. To exclude the effect of

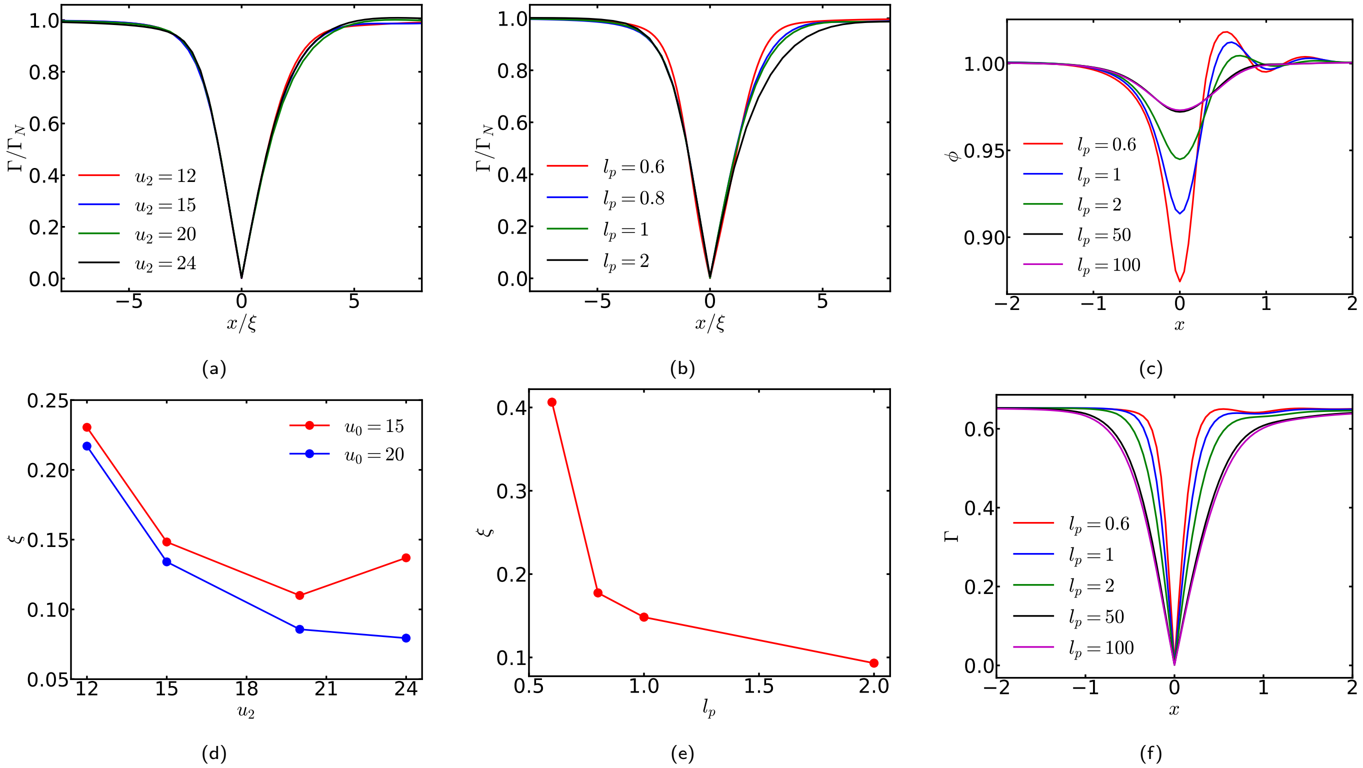

Fig. 8 Normalized optical retardance Γ/Γ_N as a function of position along the line $y=0$ for $-1/2$ defect at varying values of (a)u_2 and (b)l_p. Characteristic length ξ as a function of (d)u_2 and (e)l_p. For (a), (b), (d) and (e), all parameters except the one being varied are set to their default values as described in the main text. The characteristic length ξ for $u_2=24, u_0=15$ appears anomalous due to its coupling to a wide density variation, thus points of $u_0=20$ are added for comparison. (c), (f): Density (ϕ) and optical retardance (Γ) along the line $y=0$ for $-1/2$ defect at varying values of l_p, where $u_0=50$ to make the systems close to the incompressible limit, and u_2 are adjusted to make the $\Gamma_N \approx 0.652$($u_2=22$ for $l_p=0.6$; $u_2=15$ for $l_p=1$; $u_2=9.8$ for $l_p=2$; $u_2=5.46$ for $l_p=50$; $u_2=5.4$ for $l_p=100$).

Γ_N and compressibility on the core size, we chose $u_0=50$ and set u_2 in order to make $\Gamma_N \approx 0.652$ for various l_p. The density and optical retardance profiles along the line $y=0$ are shown in Fig.8c and 8f. The results for incompressible systems with fixed Γ_N closely resemble those observed for the interfacial widths. For rigid chains, both the interfacial widths and the core sizes are on order of L_c. As the chains become more flexible, these length scales decrease and scale with the persistence length l_p instead. We now compare our results with experimental observations of disclinations in polymer liquid crystals[37] and lyotropic chromonic liquid crystals[24]. Typically, both the contour and the persistence lengths in these systems are on the order of tens of nanometers. However, the observed core sizes in experiments are significantly larger—approximately one micrometer for polymer liquid crystals and ten micrometers for lyotropic chromonic liquid crystals. The larger core sizes observed in experiments, compared to our model predictions, may be attributed to polydispersity and self-assembly effects, which will be the focus of future investigations.

6 Conclusions

In this article, we have studied the equilibrium isotropic-nematic phase transition, isotropic-nematic interfaces, and topological defects in the nematic phase of a worm like chain liquid crystal by using Self-Consistent Field Theory. For homogeneous states, the phase transition follows by numerical minimization of the free energy functional, revealing the effects of chain number density and flexibility on the transition. Larger density or stiffer chains are associated with lower MS interaction strength at the transition point. In the case of an isotropic-nematic interface, we have studied the effects of compressibility, interaction strength u_2, and chain flexibility on the interface. A larger value of u_0 corresponds to a smaller compressibility, leading to a smaller density gap between the two phases. In the canonical ensemble, the value of u_2 determines the relative portion of the system occupied by the isotropic and nematic phases. The interfacial width increases as the chain become stiffer, as given by larger persistence length l_p and elastic constants. Both homeotropic and planar alignments have been studied. In contrast to homeotropic alignment, planar alignment displays nonzero biaxiality across the interface and a smaller interfacial width. We have also studied the equilibrium configurations associated with $\pm 1/2$ disclinations in a thin film geometry (two dimensional variations of the nematic order parameter, but allowing out of plane director orientation). Defects display a region of biaxial order in the core region, and a uniaxial center defined as the point in which $S=P$, the uniaxial and biaxial order parameters coincide. Elastic anisotropy, which is naturally incorporated in the flexible chain model, leads to an anisotropic core in agreement with previous experiments and computation. Finally, we have examined the dependence of the core structure and extent on the interaction coefficients u_0 and u_2, as well as on chain flexibility. As the system becomes less compressible, the core radius decreases and eventually plateaus in the incompressible limit. The MS interaction parameter u_2 and ratio L_c/l_p affects the core sizes by controlling the order parameter difference between the nematic region and the core center. In incompressible limit and for fixed far field nematic order S_N, the core size is seen to be on order of L_c for rigid chains, and it decreases as the chains become flexible. This model predicts a disclination core size smaller than that observed cores in lyotropic chromonic liquid crystals, which may be attributed to polydispersity and self-assembly effects. There are existing studies on equilibrium polymers based on the Gaussian chain model, where the chain length distribution is determined by chemical equilibrium[2]. A similar approach can be extended to the worm-like chain model, thereby offering a potential method for investigating lyotropic chromonic liquid crystals and other self-assembling systems. The model presented in this work can also be applied to rod-like molecular systems by taking the limit $l_p \to \infty$. Additionally, by implementing appropriate boundary conditions, the model is suitable for studying systems under confinement[6,26].

Conflicts of interest

There are no conflicts of interest to declare.

Data availability

The Python code used for this study can be found at Zenodo https://doi.org/10.5281/zenodo.14927168.

Acknowledgements

This research has been supported by the National Science Foundation under contract DMR-2223707, by the Minnesota Supercomputing Institute of the University of Minnesota, and by the Advanced Cyberinfrastructure Coordination Ecosystem: Services & Support (ACCESS) program, which is supported by U.S. National Science Foundation grants 2138259, 2138286, 2138307, 2137603, and 2138296.

Notes and references

1 G. H. Fredrickson, V. Ganesan and F. Drolet, *Macromolecules*, 2002, **35**, 16–39.

2 G. H. Fredrickson, *The Equilibrium Theory of Inhomogeneous Polymers*, Oxford University Press, 2006.

3 W. Song, P. Tang, H. Zhang, Y. Yang and A.-C. Shi, *Macromolecules*, 2009, **42**, 6300–6309.

4 Y. Jiang and J. Z. Chen, *Macromolecules*, 2010, **43**, 10668–10678.

5 M. Deng, Y. Jiang, H. Liang and J. Z. Chen, *Macromolecules*, 2010, **43**, 3455–3464.

6 R. K. Spencer, N. Saeidi and B.-Y. Ha, *The Journal of Chemical Physics*, 2020, **152**,.

7 J. V. Selinger, *Introduction to the theory of soft matter: from ideal gases to liquid crystals*, Springer, 2016.

8 X. Yao, H. Zhang and J. Z. Chen, *Physical Review E*, 2018, **97**, 052707.

9 X. Yao, L. Zhang and J. Z. Chen, *Physical Review E*, 2022, **105**, 044704.

10 S. Zhou, Y. A. Nastishin, M. M. Omelchenko, L. Tortora, V. G. Nazarenko, O. P. Boiko, T. Ostapenko, T. Hu, C. C. Almasan, S. N. Sprunt, J. T. Gleeson and O. D. Lavrentovich, *Phys. Rev. Lett.*, 2012, **109**, 037801.

11 S. Zhou, *Lyotropic Chromonic Liquid Crystals*, Springer, 2017.

12 C. F. Dietrich, P. J. Collings, T. Sottmann, P. Rudquist and F. Giesselmann, *Proceedings of the National Academy of Sciences*, 2020, **117**, 27238–27244.

13 J. Jeong, Z. S. Davidson, P. J. Collings, T. C. Lubensky and A. Yodh, *Proceedings of the National Academy of Sciences*, 2014, **111**, 1742–1747.

14 K. Nayani, R. Chang, J. Fu, P. W. Ellis, A. Fernandez-Nieves, J. O. Park and M. Srinivasarao, *Nature communications*, 2015, **6**, 8067.

15 Z. S. Davidson, L. Kang, J. Jeong, T. Still, P. J. Collings, T. C. Lubensky and A. Yodh, *Physical Review E*, 2015, **91**, 050501.

16 J. X. Velez, Z. Zheng, D. A. Beller and F. Serra, *Soft Matter*, 2021, **17**, 3848–3854.

17 L. Myers and J. Viñals, *Chiral ground states in a nematic liquid crystal confined to a cylinder with homeotropic anchoring*, 2025, `https://arxiv.org/abs/2502.15083`.

18 R. Zhang, N. Kumar, J. L. Ross, M. L. Gardel and J. J. De Pablo, *Proceedings of the National Academy of Sciences*, 2018, **115**, E124–E133.

19 B. L. Cook and P. W. Alford, *Integrative Biology*, 2023, **15**, zyad009.

20 S. M. Faisal, J. E. Clewner, B. Stack, M. L. Varela, A. Comba, G. Abbud, S. Motsch, M. G. Castro and P. R. Lowenstein, *Advanced Science*, 2024, **11**, 2309796.

21 S. Varytimiadou, D. Revignas, F. Giesselmann and A. Ferrarini, *Liquid Crystals Reviews*, 2024, **12**, 57–104.

22 A. Ghosh, Q. MacPherson, Z.-G. Wang and A. J. Spakowitz, *The Journal of Chemical Physics*, 2022, **157**,.

23 T. Odijk, *Liquid Crystals*, 1986, **1**, 553–559.

24 S. Zhou, S. V. Shiyanovskii, H.-S. Park and O. D. Lavrentovich, *Nature Communications*, 2017, **8**, 14974.

25 C. D. Schimming and J. Viñals, *Physical Review E*, 2020, **102**, 010701.

26 J. Z. Chen, *Progress in Polymer Science*, 2016, **54**, 3–46.

27 H. H. Homeier and E. O. Steinborn, *Journal of Molecular Structure: THEOCHEM*, 1996, **368**, 31–37.

28 K. C. Daoulas, D. N. Theodorou, V. A. Harmandaris, N. C. Karayiannis and V. G. Mavrantzas, *Macromolecules*, 2005, **38**, 7134–7149.

29 L. Qing, *Python Code for Numerical Solution of the Self- Consistent Field Theory in a Semiflexible Polymer Nematic*, 2025, `https://doi.org/10.5281/zenodo.14927168`.

30 Z. Y. Chen and J. Noolandi, *Physical Review A*, 1992, **45**, 2389.

31 S.-M. Cui, O. Akcakir and Z. Y. Chen, *Physical Review E*, 1995, **51**, 4548.

32 V. Popa-Nita, T. Sluckin and A. Wheeler, *Journal de Physique II*, 1997, **7**, 1225–1243.

33 B. Y. Drovetsky, A. J. Liu and C. Mak, *The Journal of chemical physics*, 1999, **111**, 4334–4342.

34 L. Myers, C. Swift, J. Rønning, L. Angheluta and J. Viñals, *Soft Matter*, 2024, **20**, 2900–2914.

35 C. D. Schimming and J. Viñals, *Soft Matter*, 2022, **18**, 2234–2244.

36 C. D. Schimming and J. Viñals, *Proceedings of the Royal Society A*, 2023, **479**, 20230042.

37 S. D. Hudson, J. W. Fleming, E. Gholz and E. L. Thomas, *Macromolecules*, 1993, **26**, 1270–1276.

The Python code can be found at Zenodo with https://doi.org/10.5281/zenodo.14927168.